ORIGINAL ARTICLE

Design and manufacturing of a surface plasmon resonance sensor based on inkjet 3D printing for simultaneous measurements of refractive index and temperature

Lorena Saitta[1] · Francesco Arcadio[2] · Giovanni Celano[1] · Nunzio Cennamo[2] · Luigi Zeni[2] · Claudio Tosto[1] · Gianluca Cicala[1,3]

Abstract

In this work, a surface plasmon resonance (SPR) multiparameter sensor for simultaneous determination of refractive index and temperature was manufactured through a novel and low-cost approach. Monitoring these parameters is useful when bio-sensors are developed by exploiting SPR phenomena. A polymer planar optical structure was realized via inkjet 3D printing, by using photo-curable resins having tailored refractive index for device's core and cladding, respectively. The multiparameter sensor was fully designed, manufactured, and experimentally tested to check the numerical analyses run on a preliminary phase. In such a way, a temperature resolution equal to about 0.5 °C and a refractive index resolution equal to about 2×10^{-4} RIU (refractive index unit) were obtained. Next, even a quality control analysis of the 3D printed surface was carried out by following a novel approach that relies on the profile monitoring technique, with the aim to evaluate the suitability of the design and the geometric accuracy control. In addition, thanks to the cost analysis performed through a properly model, it was proved that the multiparameter sensor designed, manufactured, and tested satisfies the low-cost requirements, being the estimated cost ~ 23 €, which is an absolutely competitive cost if compared with other traditional sensors. In the end, even the performance of the sensor in terms of bulk sensitivity (equal to about 900 nm/RIU) resulted to be higher than similar devices already presented in the state-of-the-art, thus proving the validity of the developed SPR multiparameter sensor both in economic and performance terms.

Keywords Additive manufacturing · Quality monitoring · Polymers · Sensor design · Plastic optical fibers

1 Introduction

The simultaneous measurement of refractive index (RI) and temperature plays a crucial role in several application fields, like for instance in biochemical sensing, such as in

Lorena Saitta and Francesco Arcadio contributed equally to this work.

✉ Lorena Saitta
lorena.saitta@phd.unict.it

Francesco Arcadio
francesco.arcadio@unicampania.it

Giovanni Celano
giovanni.celano@unict.it

Nunzio Cennamo
nunzio.cennamo@unicampania.it

Luigi Zeni
Luigi.ZENI@unicampania.it

Claudio Tosto
claudio.tosto@unict.it

Gianluca Cicala
gianluca.cicala@unict.it

1 Department of Civil Engineering and Architecture, University of Catania, Viale Andrea Doria 6, 95125 Catania, Italy

2 Department of Engineering, University of Campania Luigi Vanvitelli, Via Roma 29, 81031 Aversa, Italy

3 INSTM-UDR CT, Viale Andrea Doria 6, 95125 Catania, Italy

environmental monitoring, food quality, and point-of-care test (POCT). In fact, the refractive index solution is highly influenced by the ambient temperature. At the same time, the binding properties (e.g., the affinity constant, kinetic) strongly depend on the external temperature conditions. For this reason, the contemporaneous determination of these parameters becomes a fundamental task since, by monitoring and so compensating the temperature effect, it is possible to improve the measurement process accuracy and reliability [1, 2].

In literature, numerous experimental configurations that perform this kind of measurements, like the ones based on interferometers [3–5], no-core optical fibers [6, 7], fiber Bragg and long period gratings [8–10], and many others [11–14], are present.

Among all the others, surface plasmon resonance (SPR) is often utilized as physical phenomenon to measure both refractive index and temperature at the same time [15–18]. For instance, Liu et al. have recently presented a plasmonic parallel polished plastic optical fiber (POF) where a polydimethylsiloxane (PDMS) layer acts as thermosensitive material [19]; along the same line, Wang et al. have developed a platform based on double-sided photonic crystal fibers (PCFs) in which an arc groove covered with gold and filled with chloroform acts as thermosensitive channel, whereas a distinct channel with silver performs RI measurements [20].

Nowadays, the traditional configuration for commercial or bench-top SPR biosensor is the prism-coupled one. Although this approach is sensitive, robust, and simple, it is not suitable for miniaturization and integration [21]. For this reason, the alternative approach based on planar optical waveguide structure is taking hold in this field. Moreover, since the use of SPR sensor is moving beyond simple laboratory applications, ease of manufacture combined with low-costs and reliability are required. Commonly, injection molding allows to satisfy these requirements [22–24]. In addition to the latter, even other fabrication techniques are also commonly used to realize SPR sensor, i.e., Laser–LIGA technique [25], hot embossing technique [26], computer numerical control machining technology [27, 28], and PDMS molding technique [28]. However, even the 3D printing technique turns out to be promising for the optical waveguide fabrication, allowing the rapid fabrication of digital geometry into physical form with micron accuracy [29]. 3D printing was used for the first time to fabricate a POF in 2015 [30]. Several are the materials which have been used for the scope. At first, common filaments like acrylonitrile butadiene styrene (ABS) and polyethylene terephthalate glycol (PETG) were used, since they were commoditized and easily accessible. However, they have scarce optical properties and high loss. Thus, at a later time, optical grade resins with lower material losses, i.e., cyclic olefin polymer (COP), poly(methyl

methacrylate) (PMMA), polycarbonate (PC), and polystyrene (PS) have been used to 3D print POF [31]. In this way, it was possible to improve the POFs' optical properties, approaching the performance of the material that represents the gold standard for the SPR sensors manufacturing, that is glass.

Starting from the state-of-the-art information discussed so far, we propose a novel SPR sensor based on an inkjet 3D printed waveguide and photocurable resins, in which two distinct channels are derived for simultaneous determination of refractive index and temperature. A similar manufacturing process has been already used to build an SPR sensor based on a single channel [32]. In particular, the used 3D printed photocurable resin is a transparent material that simulates the waveguide's cladding. In addition, to fulfill the waveguide's working principle, the latter was properly combined with a photocurable optical adhesive, which was used to realize the core. In fact, to obtain a performing waveguide, the refractive indexes of the used materials for manufacturing are important parameters to be taken into account: the core and cladding must have higher and lower refractive index values, respectively [31].

In the end, when working in the manufacturing of photonic devices and optical fibers, a further issue must be taken into consideration: currently, the major loss in POFs is due to the poor control over core symmetry [31]. Thus, since in this study the core geometry is defined from a planar 3D printed substrate having a channel equal to 1×1 mm^2, a quality control of the 3D printed surface was carried out. Within the manufacturing processes, quality control's methods may include different activities with related various scopes, such as ensuring the correctness of designed 3D CAD models, verifying prepared process data, and performing visual product control [33]. On the same line, in this work, the authors focused on controlling the correctness of designed 3D CAD models based on the 3D printing machine's dimensional accuracy, which is a known data. Generally, comprehensive results can be collected by carrying out this kind of geometric accuracy analysis using volume-based methods, like computed tomography (CT) [34–36]. However, these procedures require specialized equipment and are also expensive and time-consuming. For this reason, a novel and cost-effective quality control approach is proposed from the authors: it is based on a previous profile monitoring study run by M. A. Mahmoud and W. H. Woodall in 2004 [37].

Briefly, in this experimental work:

- an innovative approach, based on inkjet 3D printing, opens the way to new manufacturing strategies on planar SPR multiparameter sensors fabrication;
- an SPR sensor with two different channels properly tailored with gold, silver, and thermosensitive polymer coatings for carrying out simultaneous measurements

of refractive index and temperature has been properly designed and manufactured;

- a wide experimental campaign was run in order to verify how it works if compared with similar devices already existent and realized through different manufacturing technologies;
- a cost-effective *quality monitoring* approach, based on profile monitoring of geometric profiles by means of control charts, was carried out to monitor the stability of the 3D printing process. The selected technique, originally proposed in literature for the Phase I implementation of control charts in a long run manufacturing process, has been adapted to the small run scenario, which characterizes the production of the investigated device.

The paper is organized as follows: Section 2 presents both the working materials (Section 2.1.) and the chosen methods to design, manufacture, and test the proposed device. The low-cost experimental setup to test the device operation by collecting simultaneous measurements of refractive index and temperature is presented in Section 2.2. Next, all information about the design and manufacturing workflow is presented in Section 2.3. The Phase I profile monitoring analysis to carry out quality control of manufactured devices is described in Section 2.4. In Section 2.5, the cost input parameters to manufacture the proposed SPR sensor are shown. The obtained results are presented in Section 3. In particular, the findings resulting from the quality control study are reported in Section 3.1. Then, the numerical and experimental results collected from the simultaneous measurements of refractive index and temperatures are shown in Sections 3.2. and 3.3, respectively, to evaluate the performance of the developed SPR multiparameter sensor. Finally, the manufacturing cost of the device is calculated in Section 3.4. Conclusions and future research directions complete the paper.

2 Materials and methods

2.1 Materials

The splitter was manufactured using two different resins: *VeroClear RGD810* and *NOA88*.

VeroClear RGD810 is an acrylic liquid photopolymer having a refractive index equal to 1.531 at 650 nm. In addition, it presents a tensile modulus equal to 2.5 GPa and a heat distortion temperature (HDT) of 45–50 °C, while it is stiff at room temperature. The formulation, which is proprietary, was developed by *Stratasys* for PolyJet 3D printing. According with the safety data sheet (SDS), it is made of a complex mixture of acrylate monomers and photoactivators. By using *VeroClear RGD810*, the splitter was 3D printed on

a 3D printer *Stratasys Objet260 Connex 1* (Stratasys, Los Angeles, CA, USA), while *FullCure705* was used as break away support material. It is a mixture of acrylic liquid photopolymer, polyethylene glycol, propane-1,2-diol, and glycerol, and it is simply removed by water jetting after printing.

The waveguide core of the 3D printed device was fabricated by filling the channel of the part with the optical adhesive *Norland Optical Adhesive NOA88*. It is a low viscosity (250cps) UV-curing adhesive with a refractive index equal to 1.56 at 589 nm. Moreover, it has an absorption range between 315 and 395 nm; hence, it was UV-cured by using a universal lamp bulb with UVA emission (365 nm).

VeroClear RGD810 and *FullCure705* were purchased from OVERMACH S.p.A. (Parma, Italy). While, *Norland Optical Adhesive NOA88* was purchased from Edmund Optics LTD (UK).

Positive PMMA E-Beam Resists AR P 679.04 was purchased from AllResist GmbH (Strausberg, Germany). It was used as thermosensitive materials by realizing a coating of the multiparameter sensor, thus allowing measurements of temperature.

2.2 Testing experimental setup

To test the proposed multiparameter sensor, a simple and low-cost experimental setup has been implemented, as shown in Fig. 1. In particular, it consists of a halogen lamp as white light source (model HL-2000LL, manufactured by Ocean Insight, Orlando, FL, USA) and a spectrometer (model FLAME-S-VIS–NIR-ES, manufactured by Ocean Insight, Orlando, FL, USA). Finally, two plastic optical fiber (POF) patches, having a total diameter equal to 1 mm, have been used to launch the light at the input and collect it at the sensor's output, respectively.

2.3 Multiparameter sensor design and manufacturing process

The multiparameter sensor was realized by designing four different parts which were then assembled. The solid model of each part of the assembly was designed with Autodesk® Fusion 360. The four parts' axonometric views are shown in Fig. 2, while each 3D printed part and the final assembly of the sensor are shown, respectively, in Fig. 3a and b.

The geometry of the substrate (bottom part) was designed starting from a previous design [29], but applying some modifications needed for the purpose. This part was modeled with a central channel having a square section of dimension equal to 1.2×1.2 mm^2, which branches off into two different arms. These ones, in turn, are converge to a single output channel at the opposite end of the device. The channel's dimension in the CAD model has been selected as to account for the accuracy of the 3D

Fig. 1 Experimental setup used to test the multiparameter sensor
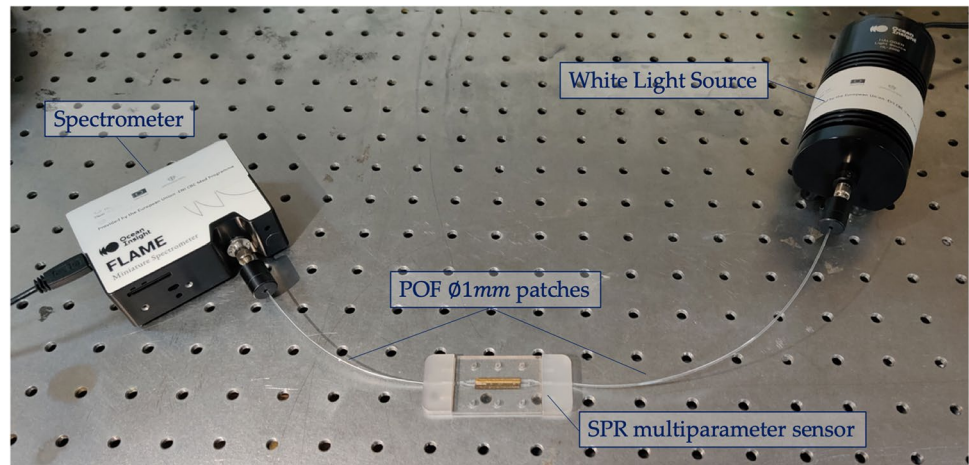
Fig. 2 Axonometric view of the substrate (**a**), cover (**b**), mask (**c**), plastic optical fibers' (POFs') support (**d**), and substrate and mask assembly with cross-section view showing the working principle for channel functionalization with noble metals (**e**)
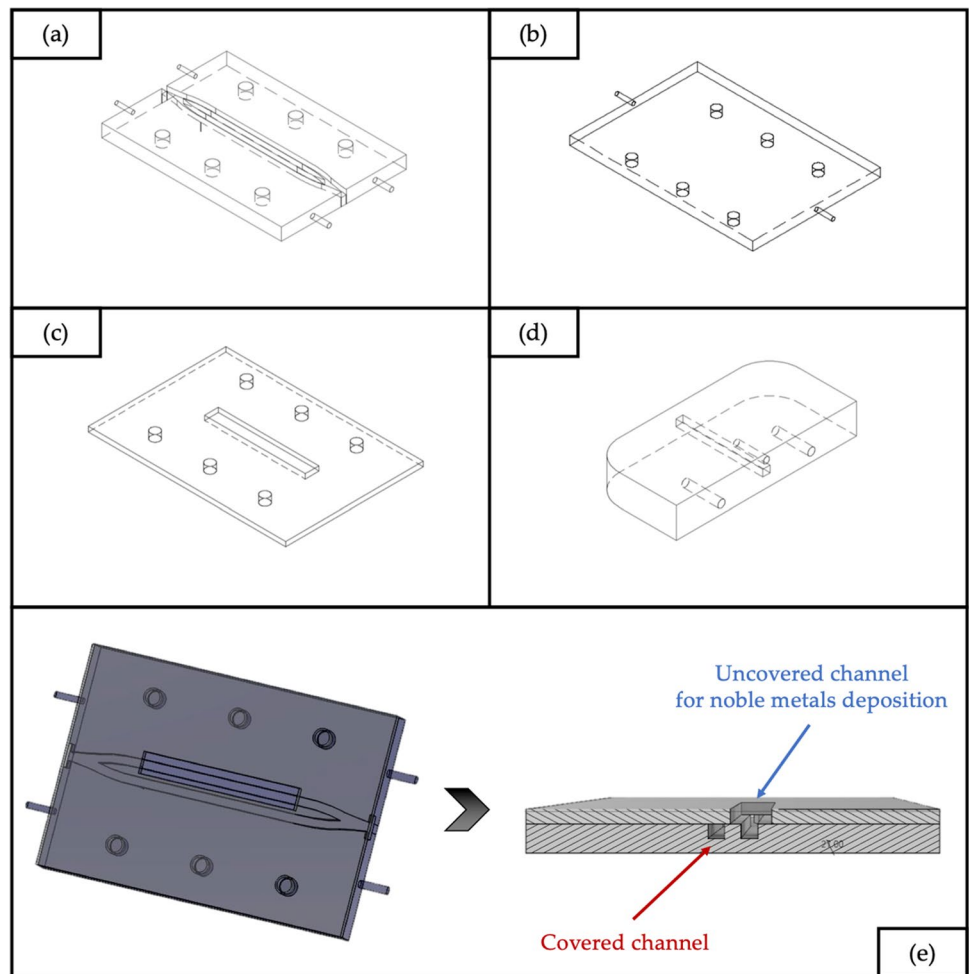

printing process manufacturing the sensor. Therefore, by design, the nominal channel's width was set equal to 1 mm. Actually, accounting for the process accuracy required an offset (bias setup) equal to 200 μm in the design phase with respect to the nominal dimension. The two branches were needed to run refractive index and temperature measures at

the same time, by sputtering them with two different noble metals. The geometry is totally defined in Fig. 4.

To insert the input/output POFs with a perfect alignment with respect to the core, customized supports were designed (Fig. 2d). In fact, three holes were designed in

Fig. 3 **a** 3D printed disassembled parts and **b** assembled SPR splitter
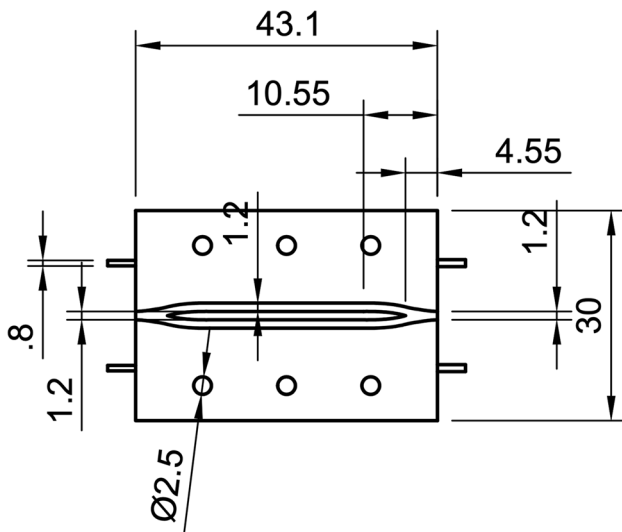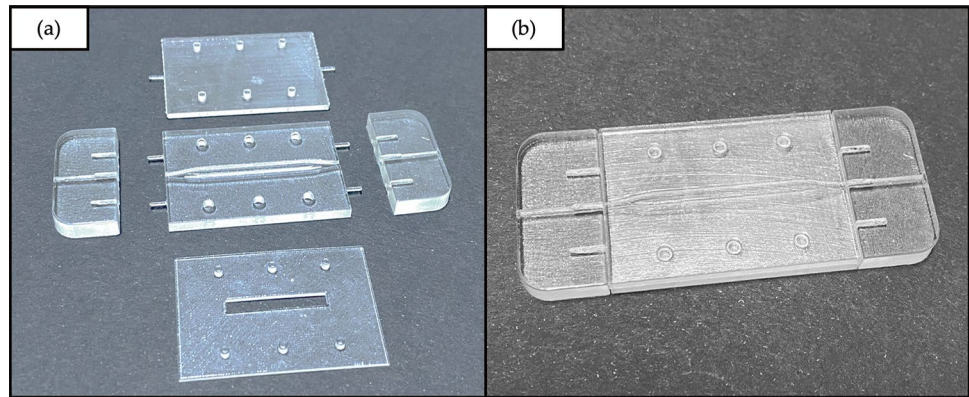
Fig. 4 Substrate geometry in phase of design. For the channel's width, a bias equal to 200 μm was set taking into account the accuracy of the 3d printing, thus obtaining the desired size

the support to perfectly fit with the substrate and cover's centering pins (Fig. 2 a and b).

Moreover, starting from the geometry of the substrate, for cladding the uncovered part of the core, a cover was designed. The fitting between the latter and substrate was ensured by predisposing a hole-pin system, as shown in Fig. 2a and b.

Finally, to trigger the SPR phenomenon, it was necessary to sputter a thin layer of two different noble metals on each arm of the channel: gold and silver. So, based on the geometry of the substrate, a customized mask was designed to sputter the two metals exclusively on the core waveguiding. In detail, the mask's window was designed having a width (3 mm) larger than the core one (1.2 mm) to avoid the presence of shadow areas during the deposition process, thus allowing to obtain a uniform coating on the optical waveguide. The working principle is schematized in Fig. 2e.

The splitter manufacturing involved several typical steps of generic additive manufacturing (AM) process. First, using *Autodesk® Fusion 360* the splitter device was designed and the STL file was generated. Next, the latter was processed, by using the proprietary software *Objet Studio™*, to create the G-Code instructions for the 3D printer. Once the build preparation was completed, the splitter creation started. This last step was accomplished by using the PolyJet 3D printer *Stratasys Objet260 Connex 1*. Thus, through an inkjet print head, small droplets of liquid photopolymer ink (*VeroClear RGD810*) were jetted on a build platform, and then, they were immediately photocured (solidified) by mean of a light source, that is a UV light. The latter comes from a UV lamp that is located on the print head itself. In this way, the fabrication process of the sensor proceeds layer-by-layer. Moreover, by following the same procedure, the support material (*FullCure705*), near complex geometries, is jetted and solidified simultaneously with the model material to guarantee the structure's stability. Each step followed to manufacture the splitter device is shown in Fig. 5.

Once the 3D printing process was finished, the core waveguide of the optical splitter was fabricated. Hence, the *NOA88* UV photopolymer adhesive was microinjected into the channel. The microinjection was performed with a syringe equipped with a needle having a gauge of 0.5 mm. To cure the photopolymer adhesive, it was irradiated for 15 min with a universal lamp bulb with UVA emission at 365 nm (Fig. 6). To avoid liquid *NOA88* spilling into the areas made for the insertion of input and output POF waveguides, these portions of the cavity were occluded with customized 3D printed tool having a quite fine surface to limit the waveguide's surface roughness.

With regard to the simultaneous measurements of refractive index and temperature, an e-beam resist nano-layer, having a thickness equal to about 220 nm, has been considered as thermosensitive material. More in detail, the production process of the multiparameter sensor can be summarized as follows: at first, a 60-nm thick gold film has been sputtered on a single channel (named as "channel 1") of the splitter,
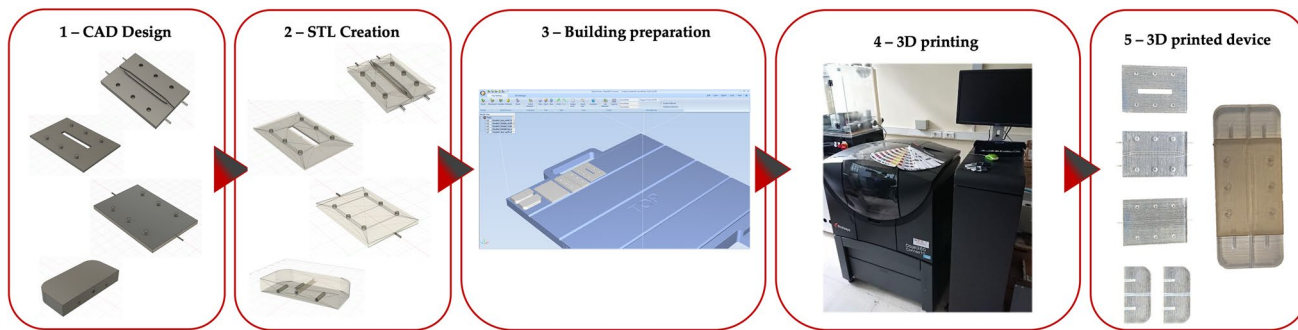
**Fig. 5** Steps pursued for the device manufacturing

Fig. 6 *NOA88* optical adhesive curing under UVA irradiation

by taking advantage of the 3D printed mask previously described; in a second step, an e-beam resist layer has been spun over the entire splitter; finally, a 40-nm-thick silver film has been sputtered on the other channel (named as "channel 2") of the splitter, once again by using the designed mask. In fact, since the design of the sensor is symmetrical with respect to the central axes parallel to both the longer and shorter sides, it was sufficient to simply rotate the mask to perform the sputter coating on channel 2 (silver sputter). A picture of the produced device, together with the schematic cross sections of each channel, has been reported in Fig. 7.

2.4 Quality monitoring of the 3D printed surfaces

For the production of disposable all-plastic devices and sensors, the inkjet 3D printing technique can be considered as

Fig. 7 Produced device for simultaneous measurements of refractive index and temperature, together with schematic cross section of the channels
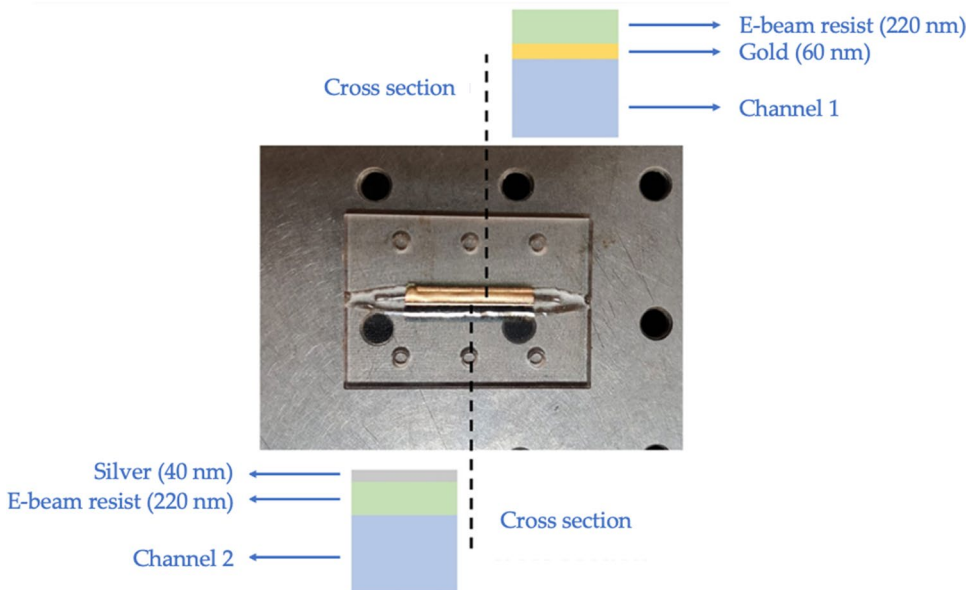
a valid alternative to silicon-based approaches, because it allows to customize and create complex shapes and geometries with high accuracy, repeatability, and resolution [38, 39]. To prove quality of manufacturing for the multiparameter sensor designed, manufactured, and tested in this study, a profile monitoring study was carried out, as proposed by M. A. Mahmoud and W. H. Woodall [37], on an pilot run of devices. The objective was testing the stability of the channels' width, which strongly influences the sensor performance. Profile monitoring has been pursued by implementing Phase I control charts aimed at checking the stability of the generated channels' profiles. A Phase I control chart is usually implemented on a finite retrospective sample (in this case, the pilot run): thus, the proposed approach fits well the 3D printing of a small run of devices. In particular, by carrying out the quality monitoring activities, two important aspects of the investigated 3D printing technology have been considered:

- the *accuracy* — i.e. how much the dimensions of the channel obtained through 3D printing are close to the nominal CAD's dimensions;
- the *precision* — i.e. the consistency of the machine, which provides an indication about the random error affecting each 3D printing manufacturing operation.

It is worth highlighting that quality *monitoring* only allows the generated profiles stability to be checked by drawing a posteriori conclusions on the parameters characterizing the generated profiles' geometry. Any further improvement on this geometry can be obtained by implementing quality *improvement* techniques, whose implementation is out of the scope of this paper and is settled in the suggested future research directions.

The 4-step procedure (see Fig. 8) to investigate the stability of observations collected for the channels' width was organized as in the following steps.

- **Step 1**. *Geometry characterization*. Since the geometry of the channel is symmetrical with respect to the central axis of the device, by using a digital microscope, appropriate images were acquired for each half of the device. Then, to get the observations of the channel's width for each manufactured device, each image showing half of device has been divided into $s = 3$ different *sections*: the rationale behind this decision was accounting for the variable geometry of the channel itself. The first section coincides with the diverging geometry within the input channel; the second section corresponds to the divergent geometry where channel splits into two branches; finally, the third section is the geometry having a constant width for the two branches. The obtained sections are illustrated in Fig. 9.
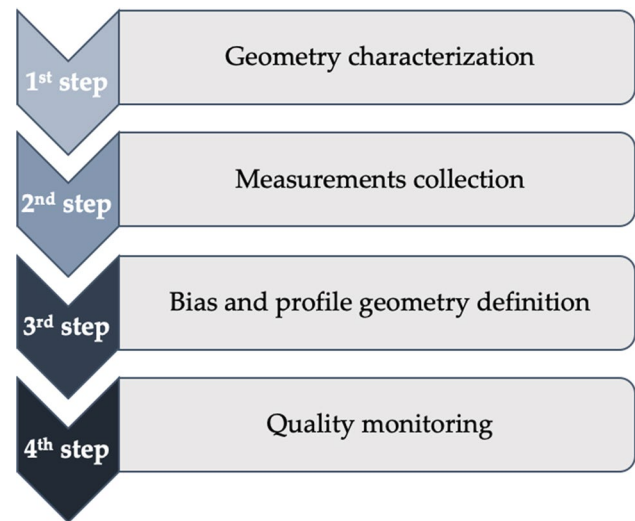
**Fig. 8** Flow chart of the implemented 4-step quality monitoring procedure

- **Step 2**. *Measurements collection*. By using the ImageJ software, the total length L_s of each identified section s, for $s = 1, 2, 3$, has been divided into a number $(n_s - 1)$ of equal parts, each having length $\Delta x = 500$ μm. For the s-th section, let us denote with $w_{ij}^{(s)}$ the measured channel's width at the i-th endpoint $x_i^{(s)}$ of each part for the j-th available profile, with $i = 1, 2, \ldots, n_s$, $j = 1, 2, \ldots, k_s$ and $s = 1, 2, 3$, see Fig. 9. The same procedure has also been carried out on the CAD model of the device by using Autodesk® Fusion 360 to collect at each i-th endpoint $x_i^{(s)}$ the values of nominal design channel's widths $W_i^{(s)}$. Therefore, for each investigated section, the following datasets of observations $w_{ij}^{(s)}$ have been gathered:

  - 1st section ($s = 1$) — section length: $L_1 = 3$ mm, width observations (sample size): $n_1 = 7$; number of profiles: $k_1 = 8$; total number of observations: $N_1 = 56$;
  - 2nd section ($s = 2$) — section length $L_2 = 5.5$ mm, width observations (sample size): $n_2 = 12$; number of profiles: $k_2 = 11$; total number of observations: $N_2 = 132$;
  - 3rd section ($s = 3$) — section length $L_3 = 5.5$ mm, width observations (sample size): $n_3 = 12$; number of profiles: $k_3 = 12$; total number of observations: $N_3 = 144$.

- **Step 3**. *Bias and profile geometry definition*. The observed 3D printing process accuracy (bias) $y_{ij}^{(s)}$ at each abscissa $x_i^{(s)}$ was calculated as the deviation of each width observation from the nominal channel's width:

Fig. 9 Splitting the sensor's waveguide into $s = 3$ contiguous sections, each characterized by its own geometric complexity. All sections' lengths L_s, $s = 1, 2, 3$, are divided into equal parts, each having length $\Delta x = 500\ \mu m$
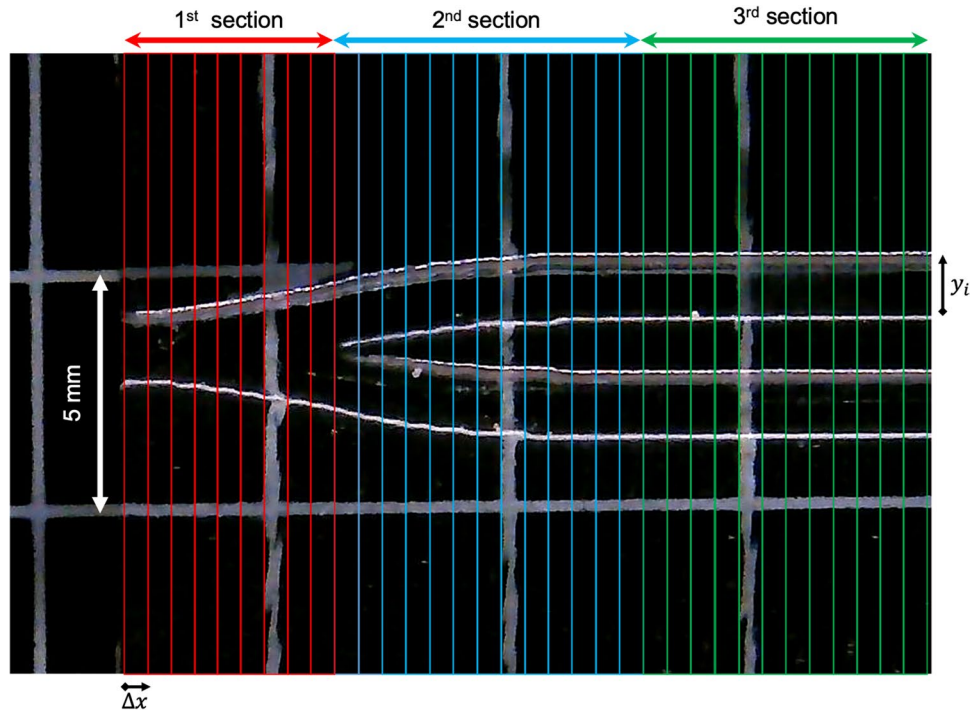
$$y_{ij}^{(s)} = W_i^{(s)} - w_{ij}^{(s)}$$

for $i = 1, 2, \dots n_s$, $j = 1, 2, \dots, k_s$ and $s = 1, 2, 3$.

Therefore, for the j-th profile collected over time at section s, there are n_s couples $\left(x_i^{(s)}, y_{ij}^{(s)}\right)$, for $i = 1, 2, \dots n_s$, $j = 1, 2, \dots, k_s$ and $s = 1, 2, 3$. Assuming a linear model relating the abscissa $X_i^{(s)}$ to the bias $Y_{ij}^{(s)}$, we get:

$$Y_{ij}^{(s)} = A_{0j}^{(s)} + A_{1j}^{(s)} X_i^{(s)} + \varepsilon_{ij}^{(s)} \tag{1}$$

where $\varepsilon_{ij}^{(s)} \sim N\left(0, \sigma_j^{(s)2}\right)$ is the random error at each section, which accounts for the 3D printing precision. If the width bias is stable, then $A_{0j}^{(s)} = A_0^{(s)}$, $A_{1j}^{(s)} = A_1^{(s)}$ and $\sigma_j^{(s)} = \sigma^{(s)}$, for $s = 1, 2, 3$, $j = 1, 2, \dots, k_s$.

- **Step 4**. *Quality monitoring*. For each section s, with $s = 1, 2, 3$, we have checked the accuracy and precision of 3D printing by performing a Phase I linear profile study according to the method proposed by Mahmoud and Woodall (2004) [37], which compares several regression lines to identify the presence of out-of-control profiles. Firstly, the proposed method implements a univariate control chart to check the stability of the error variance (monitoring the precision of 3D printing) $\sigma_j^{(s)}$, for $s = 1, 2, 3$, $j = 1, 2, \dots, k_s$. This chart plots the residual mean squared error $MSE_j^{(s)}$, for $s = 1, 2, 3$, $j = 1, 2, \dots, k_s$, from each model vs a control interval. Then, the method performs a multiple regression lines study based on a F statistic to check for the stability of the regression parameters (monitoring the accuracy of

3D printing). A detailed description of formulas used in the proposed method is not reported here for the sake of brevity and can be found in Mahmoud and Woodall (2004).

The accuracy declared by the 3D printing machine manufacturer fixes an upper specification limit for the bias error equal to $USL = 200\mu m$.

2.5 Background and protocol of the measurements

The performances of the developed sensor, in terms of temperature sensing, were evaluated by determining two different parameters, i.e., the sensitivity (S) and the resolution (ΔT). The former was determined by evaluating the ratio among the variation in the measured parameter (δM), that is the resonance wavelength or intensity at the resonance wavelength, caused by a variation of the temperature for the encompassing medium (δT). So, we get:

$$S = \frac{\delta M}{\delta T} \tag{2}$$

Whilst, the latter parameter was evaluated as follow:

$$\Delta T = \frac{\delta T}{\delta M} \delta E = \frac{1}{S} \delta E \left[°C\right] \tag{3}$$

where δE is the max experimentally measured variation of the considered parameter. A similar approach can be used

to evaluate the sensor performances in the refractive index measurements.

To carry out the temperature measurements for the sensor, at first it was tested by using water at room temperature (18 °C) as encompassing medium for both the channels. Then, the sensor was tested by conducting experimental measurements at various temperatures of the surrounding medium (from 18 up to 30 °C). During this experimental process, the solution's temperature was monitored through a thermocouple having a resolution of 0.1 °C (RS 206–3750. Corby, UK).

While to run the refractive index measurements, the sensor was tested by using several water/ethanol solutions characterized by various refractive index values ranging between 1.332 and 1.350. The refractive index value for each used solution was measured by exploiting an Abbe refractometer (Model RMI, Exacta + Optech GmbH, Munich, Germany).

2.6 CTE evaluation for PMMA layer

By varying the external solution temperature where the SPR multiparameter sensor was tested, the ultra-thin PMMA layer expands, so reducing in turns its refractive index value. To prove this phenomenon, the thermal expansion of the PMMA layer was properly evaluated. In detail, to achieve this aim, it used the definition of the coefficient of thermal expansion (CTE) as property of the material, i.e.:

$$CTE = \frac{1}{l}\frac{\Delta l}{\Delta T} \tag{4}$$

being ΔT the change of temperature which cause the sample's variation in length Δl, which before the thermal expansion phenomenon has an initial length l. The *CTE* evaluation was carried out by using a previous study of W. D. Drotning et al. [40], where the effect of the moisture content on the *CTE* of PMMA was demonstrated. In particular, they have experimentally defined a function which provide an expression for the *CTE* against the % weight gain (W) once the PMMA is immersed in water and temperature (T) expressed in (°C) as follows:

$$CTE\left(\frac{1}{°C} \times 10^{-6}\right) = 59.3 + 4.26W + 0.222T + 0.139WT \tag{5}$$

Thus, by immersing the PMMA sample in water, the parameter W was empirically determined. Moreover, by using the Eq. (5) the *CTE* was evaluated for different values of interests of temperature (T).

2.7 Cost modelling

A cost model was implemented to evaluate the cost of the 3D printed splitter. Similar to our previous work [32], the cost parameters were categorized as material costs, machine costs, and process costs. In Table 1, the input parameters used to evaluate the final device cost are itemized. Going more deeply, it was considered both the raw materials costs and their related consumption to manufacture the designed splitter. Next, being known the purchase, installation, and maintenance costs of the 3D printing used, the depreciation of the machine was considered. Moreover, being known the building time for all the parts of the 3D printed splitter, the power costs were evaluated, while labor cost was not taken into account, since the operator has spent few minutes during the start printing step and to remove the part from the building platform at the end of the 3D printing process.

3 Results and discussion

3.1 Quality monitoring: Phase I study.

In this section, we show the obtained results from the Phase I linear profile study for section $s = 1$. Detailed results concerning other sections are available upon request by authors. Figure 10 a shows the regression models fitting the abscissa $X_i^{(1)}$ to the bias $Y_{ij}^{(1)}$.

For section $s = 1$, all collected measures of width bias are below the maximum bias error $USL = 200\mu m$. Similar results have also been obtained for the other sections. The control chart monitoring the $MSE_j^{(1)}$ vs profile j, for $j = 1, 2, \ldots, k_1$, is shown in Fig. 10b: the control limits are equal to (LCL, UCL) = (0 μm, 200 μm). Each circle point plotted on the control chart has a value corresponding to a profile's $MSE_j^{(1)}$. The control chart reveals that all points are within control limits, thus proving that the 3D printing machine precision is under control. After eliminating some out-of-control points, the same result is also achieved for sections $s = 2, 3$.

Table 1 Cost model input parameters

Input parameters		Unit	Value
Material	VeroClear RGD810	€/kg	393.11
	FullCure705	€/kg	126.74
	Norland Optical Adhesive NOA 88	€/ml	2.50
Part	Model	kg	0.024
	Support	kg	0.013
	Printing time	h	0.63
	Optical adhesive	ml	2.00
Machine	Depreciation cost	€/kg	10.00
Process	Power cost	€/kWh	0.10
	Labor	€/h	0
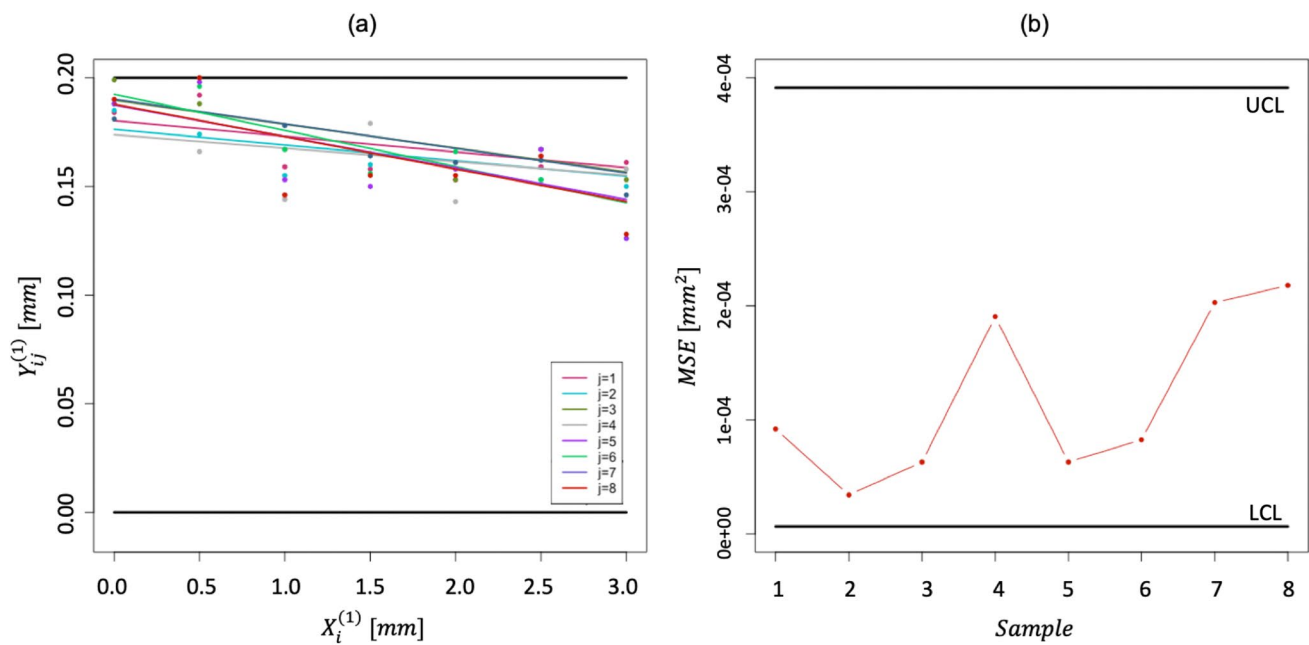
Fig. 10 **a** Observations of the channel's width bias $Y_{ij}^{(1)}$ vs $X_i^{(1)}$ and fitting regression models for each profile j, for $j = 1, 2, \ldots, k_s$. **b** Control chart for the $MSE_j^{(1)}$ vs profile j, for $j = 1, 2, \ldots, k_1$, (control limits (LCL,UCL) = (0 μm, 200 μm))

Table 2 Accuracy monitoring for each investigated section. Global F test results

Section	F-value	F_{crit}	Accuracy
1	0.835	2.213	In-control
2	10.146	1.836	Out-of-control
3	13.962	1.790	Out-of-control

The outcomes of the global F tests on multiple regression lines to prove the accuracy stability are summarized in Table 2.

Where F_{crit} is the critical value of the F test. The accuracy can be considered in-control for section $s = 1$ ($F < F_{crit}$). Conversely, it is out-of-control for sections $s = 2, 3$ ($F > F_{crit}$): this reveals a statistically significant difference among profiles generated on the investigated devices. This outcome from the ANOVA study depends on the very small values of mean squared error MSE of profiles measurements obtained for sections $s = 2, 3$. Furthermore, a deeper investigation on profiles generated at sections 2 and 3 reveals that all measurements of width bias are far below the accuracy threshold equal to $200\mu m$, with a very small precision error, (as explained by the small MSE values). This is an index of high process capability that allows for small process deviations among profiles, without having practical consequences on quality of manufactured parts. Moreover, it has been proved that the set bias equal to 200μm during the design phase was the

right one in order to obtain the desired value for the channel's width of the sensor.

3.2 Numerical results

To predict the optical response of the SPR multiparameter sensor, a *numerical study* was accomplished by exploiting a N-layer approximation and making use of the transfer matrix formalism already described in [32] to determine the influence of the thin PMMA resist layer on the channel with gold nanofilm. In particular, it was defined how on channel 1 the additional PMMA layer deposited on the gold layer affected the SPR spectra at two fixed different refractive index values, i.e., 1.332 and 1.340. In Fig. 12, the simulated numerical results both in the presence and in the absence of the PMMA top layer are shown. According with the obtained results, the presence of the polymeric layer (PMMA) produces two distinguishable resonance peaks: the first one at around 780 nm is relative to an SPR phenomenon; on the opposite, the anti-resonance peak at around 710 nm is relative to a lossy-mode resonance (LMR) phenomenon. With regard to the latter, it is important to underline that the LMR phenomenon can be excited by thin metallic oxides and polymers [40–42]. Furthermore, the spectra reported in Fig. 11 clearly denote that the anti-resonance peak is present only when the PMMA resist nano-layer is considered as an overlayer on the gold nanofilm.

Next, a second numerical simulation (similar to the one used for the results reported in Fig. 11) was carried out by

Fig. 11 Simulated SPR spectra at varying of the external refractive index relative to the SPR sensor with gold and with (or without) PMMA resist layer on top
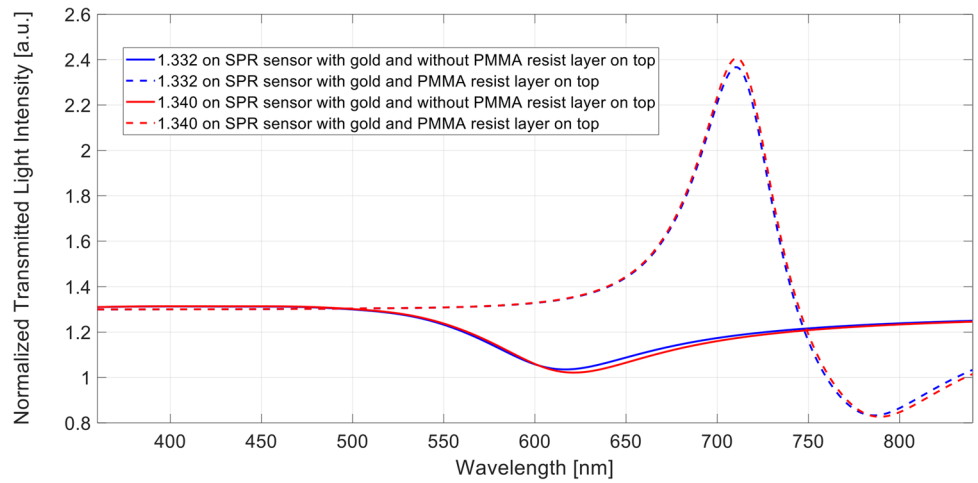
Fig. 12 Simulated SPR spectra relative to channel with silver film. Changes effects in PMMA resist under the metal film: **a** fixed refractive index value (equal to 1.50) and variable thickness (ranging from 160 to 280 nm) and **b** fixed thickness (equal to 220 nm) and variable refractive index values (ranging from 1.49 to 1.51)
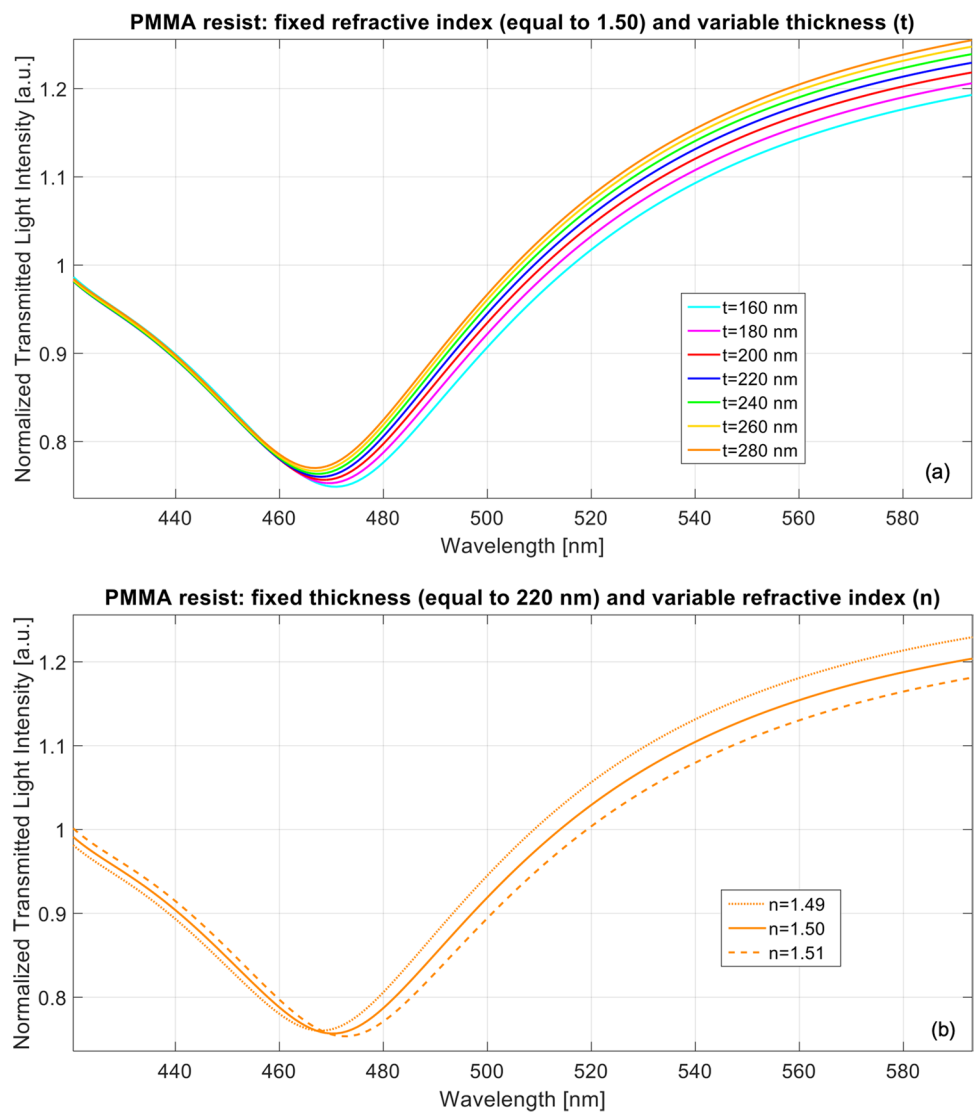
considering the channel coated with the silver film (channel 2) to determine how the resonance wavelength relative to the SPR phenomenon triggered in this channel was affected by varying either the thickness or the refractive index of the PMMA layer beneath the metal film. In Fig. 12, the SPR spectra acquired by considering both a variable thickness of the polymeric layer at a fixed nominal PMMA resist refractive index value (see Fig. 12a) and a fixed nominal thickness of the polymeric layer with a variable refractive index (see Fig. 12b) are reported. The simulated results indicate that both a reduction of the refractive index and a decreasing thickness, which is substantially equivalent to an expansion of the PMMA resist layer under the silver film, causes a blue shift of the resonance wavelength.

3.3 Experimental results

The experimental results obtained by testing the SPR multiparameter sensor with water at 18 °C are shown in Fig. 13. In detail, the normalized SPR spectrum shown in Fig. 13a was obtained by considering simultaneously the two sensitive channels and normalizing with respect to the one gathered by assuming air as surrounding medium for both the channels. As can be clearly seen, three distinguishable resonance peaks can be noticed: the first one, at about 460 nm, is relative to the SPR phenomenon on channel 2 (with e-beam resist nano-layer and silver film on the top); the second one, at about 680 nm, is relative to the SPR phenomenon on channel 1 (with gold film and e-beam resist nanolayer on the top); the third one, at about 590 nm is ascribable to the ultra-thin resist layer on the gold film and is relative to a lossy-mode resonance (LMR) phenomenon. More in detail, Fig. 13b reports the SPR spectra, acquired with water at 18 °C, obtained by using the two sensitive channels individually, i.e., one at time. As it is shown, the LMR peak is not present when considering the channel 2 (with silver) whereas it is clearly present when considering channel 1 (with gold). This aspect is in accordance with the simulation results previously discussed, since they have shown that this phenomenon is up to the ultrathin polymeric layer upon the gold nanofilm (see Fig. 12).

Fig. 13 SPR spectra acquired with water at room temperature as surrounding medium on **a** both channels and **b** channels considered once a time
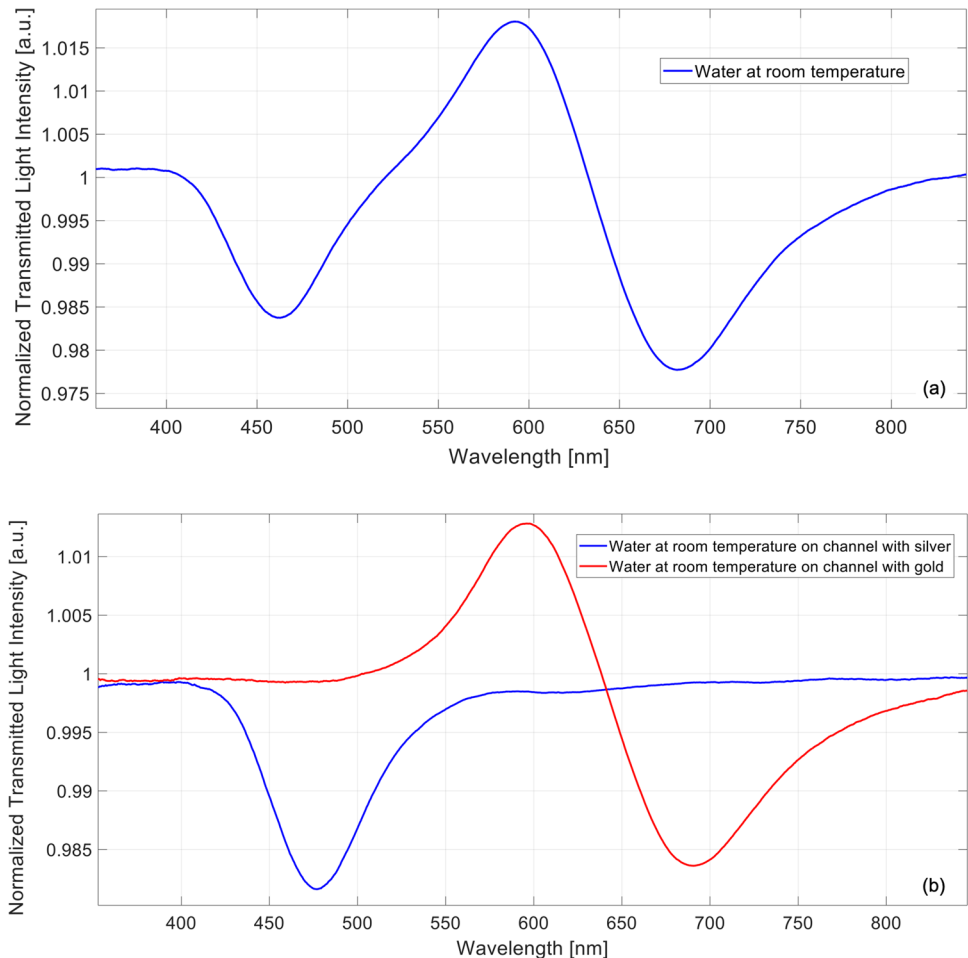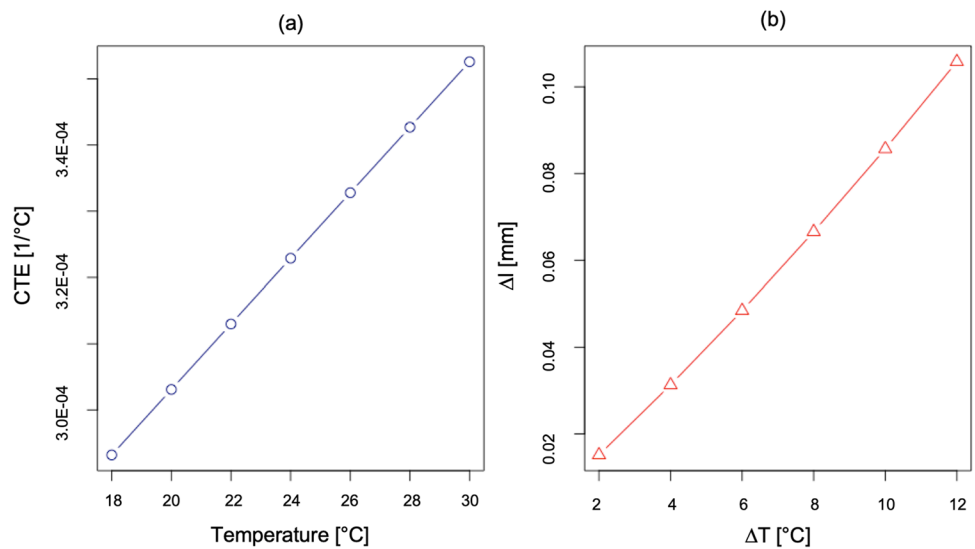
Fig. 14 SPR spectra acquired with water at different temperature values ranging from 18 to 30 °C. Inset: zoom of the resonance wavelength area relative to the peak at around 460 nm
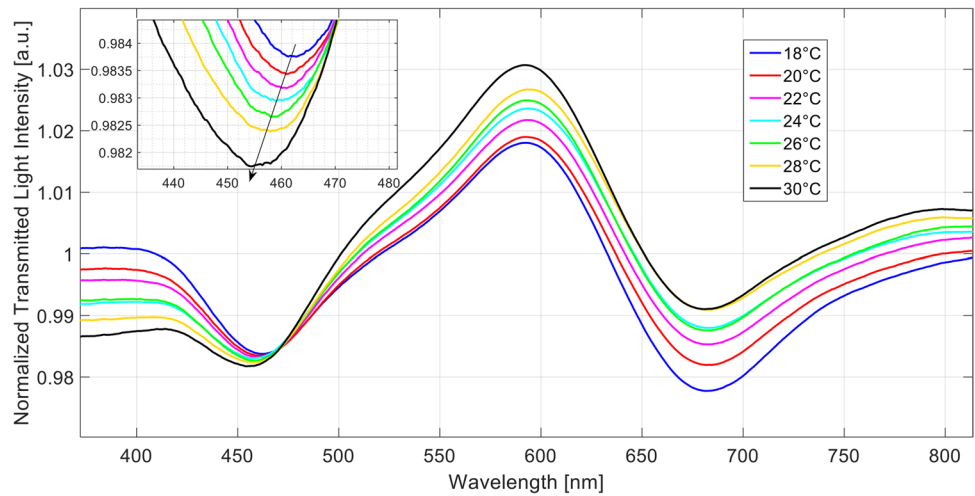
Fig. 15 **a** Estimated *CTE* values for PMMA after being immersed in water as function of the temperature, being fixed the % weight gain at 34%; **b** PMMA's expansion Δl at different ΔT values

3.3.1 Temperature measurements

The SPR spectra experimentally obtained by using the sensor for running temperature measurements at different temperature values of the water have been reported in Fig. 14. From the latter, it is possible to observe that when the water temperature changes, only the resonance peak relative to the channel with silver significantly changes. In particular, as temperature raises, the resonance wavelength (at about 460 nm) shifts toward lower values (blue shift). On the opposite, the resonance peak (at about 680 nm) relative to the channel with gold is basically not influenced by temperature variations, whereas the intensity of the peak at about 592 nm gradually increases with growing temperature values.

More specifically, at varying of the external solution temperature, the ultra-thin PMMA layer expands, so reducing its refractive index value. To confirm this aspect and to estimate the expansion of the PMMA it was used a combination

Table 3 Estimated expansion of PMMA in terms of length (Δl) for each value of *CTE* estimated through Eq. (4) and for different values of ΔT

CTE (1/°C)	ΔT(°C)	Δl(mm)
3.03E − 04	2	1.52E − 02
3.13E − 04	4	3.13E − 02
3.23E − 04	6	4.84E − 02
3.33E − 04	8	6.66E − 02
3.43E − 04	10	8.57E − 02
3.53E − 04	12	1.06E − 01

of Eqs. (4) and (5), previously defined. By immersing the PMMA sample in water, the parameter *W* (% weight gain) empirically determined was equal to 34%. Next, by using Eq. (5), the *CTE* was evaluated for different values of interests of temperature (*T*). The obtained results are plotted in

Fig. 15a. Once the *CTE* was determined for each value of temperature, the expansion of PMMA in terms of length (Δl) was calculated starting from Eq. (4) at each possible (ΔT) for the experimental testing of the multiparameter sensor designed. The obtained results are reported in Table 3, while the Δl versus ΔT plot is shown in Fig. 15b.

Thus, through the used model in Eq. (5), it was proved that by increasing the external solution temperature, the ultra-thin PMMA layer is subjected to an expansion process, since the Δl tends to increase, so reducing its refractive index value. This effect causes two distinct phenomena on the splitter channels. In fact, with regard to the channel with silver, the PMMA layer dilation under the metal film produces a remarkable blue shift of the resonance wavelength (see Fig. 14), as already demonstrated by the simulated results in Fig. 12.

On the contrary, for what concerns the channel with gold, the expansion of the PMMA resist layer above the metal film

is mainly verifiable with the anti-resonance peak at about 592 nm, whose intensity markedly changes together with a slight blue shift of the resonance wavelength value.

So, in order to monitor the solution temperature changes, it is possible to examine both the resonance wavelength variations of the peak at 460 nm and the intensity variation, considered at the resonance wavelength, of the peak at 592 nm. For both cases, Fig. 16 reports both the considered parameters, i.e., the absolute value of the resonance wavelength ($|\Delta\lambda_{460\,nm}|$) variation, and intensity variation at the resonance wavelength ($\Delta I_{592\,nm}$), calculated with respect the corresponding values obtained with water at room temperature ($T = 18\ °C$) as surrounding medium. In the view of a first-order analysis, the linear fittings of the experimental data are also reported in Fig. 16.

Moving on the sensor's performances evaluation, by using Eq. (2), in both cases, its *sensitivity* can be approximated as the slope of the linear fitting functions reported in

Fig. 16 **a** Absolute value of the resonance wavelength variation relative to the peak at 460 nm ($|\Delta\lambda_{460\,nm}|$) calculated with to respect water at room temperature ($T = 18\ °C$), as a function of the external liquid temperature with the linear fitting of the experimental data; **b** intensity variation relative to the peak at 592 nm ($|\Delta I_{592\,nm}|$) calculated with respect to water at room temperature ($T = 18\ °C$), as a function of the external liquid temperature with the linear fitting of the experimental data
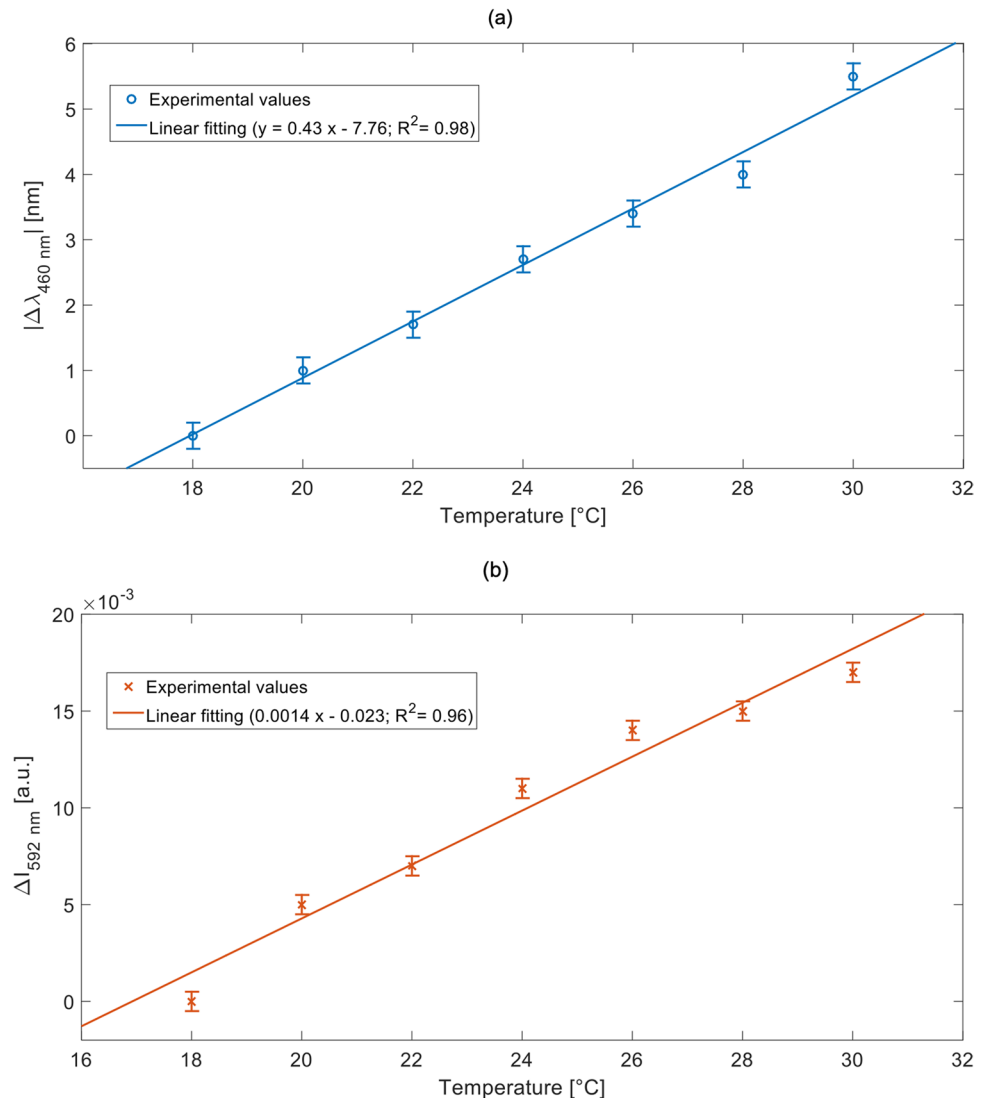
Fig. 16. In Table 4, the performance values (*sensitivity* and *resolution*) relative to both the parameters considered for the temperature measurements are summarized.

3.3.2 Refractive index measurements

With regard to the refractive index measurements carried out, the SPR spectra obtained at different refractive index values of the surrounding aqueous medium are reported in Fig. 17. As it is clear, a shift toward higher values (red shift) can be observed for each considered peak. More specifically,

since only a slight variation in resonance wavelength has been obtained with regard to the peak at 592 nm, the bulk sensitivities have been calculated in relation to the peak associated to the channel with silver (at 460 nm) and to the one related to the channel with gold (at 690 nm).

In similar way to the temperature measurements, Fig. 18 reports, for both the considered peaks, the wavelength resonance variations calculated with respect to water (n=1.332) along with the linear fitting of the experimental data. As for before, also in this case the bulk sensitivity can be approximated with the slopes of the linear fitting functions.

Table 4 Performances values relative to the resonance wavelength variation relative to peak at 460 nm and the Intensity variation at the resonance wavelength relative to peak at 592 nm

Parameter	Sensitivity (S)	Error (δE)	Resolution (ΔT)
Resonance wavelength variation relative to peak at 460 nm	0.43 (nm/°C)	0.2 (nm)	0.46 (°C)
Intensity variation at the resonance wavelength relative to peak at 592 nm	0.0014 (a.u./RIU)	0.001 (a.u.)	0.71 (°C)

Fig. 17 SPR spectra acquired with several water/ethanol solutions having a refractive index ranging from 1.332 to 1.350
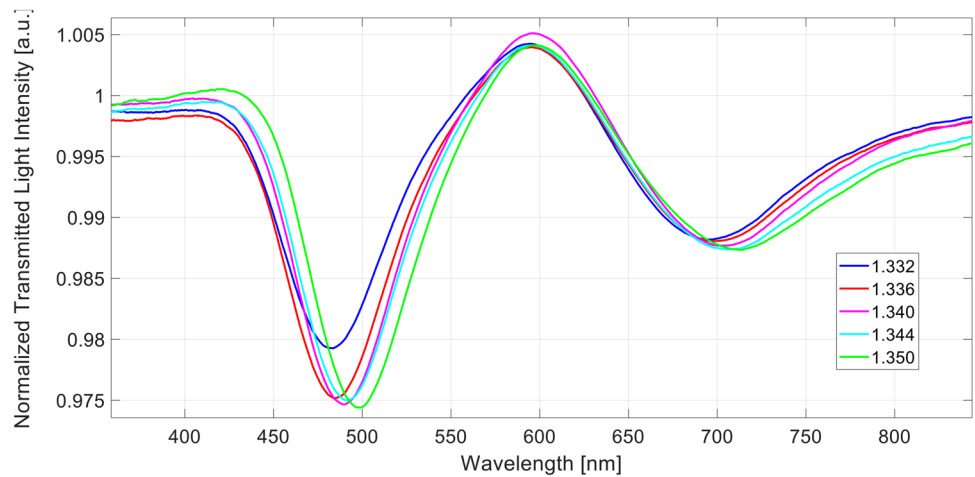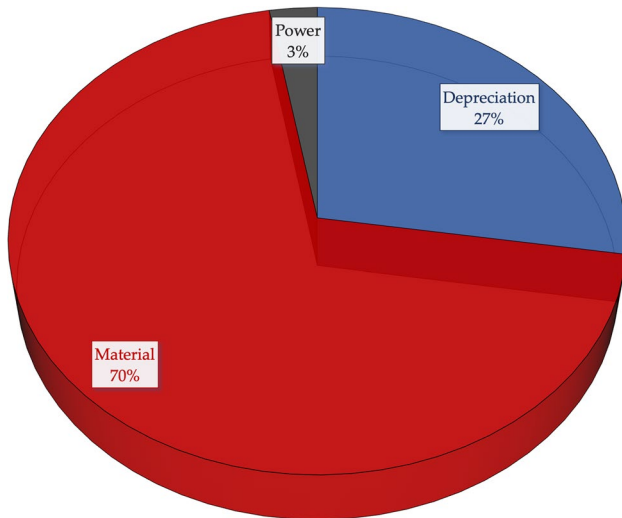

Fig. 18 Resonance wavelength variation (Δλ) calculated with respect to water (n = 1.332) with linear fitting of the experimental data relative to channel with gold and channel with silver
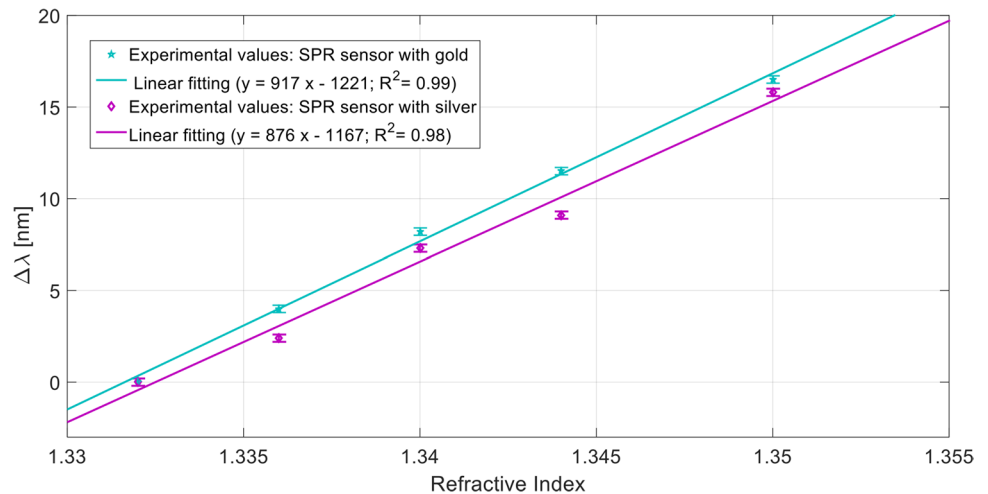
Table 5 Cost allocation and total cost evaluation

Total Cost for one Splitter	%	€
Depreciation	27	6.33
Material	70	16.08
Power	3	0.63
Total Cost		23.05

Fig. 19 Allocation of total cost

The obtained results show a similar bulk sensitivity for both channels, equal to about 880 nm/RIU for what regard the channel with silver and equal to about 920 nm/RIU in relation to the channel with gold. Both these values are higher with respect to the one calculated with a similar device based on a single channel and gold [32]. In a similar way to the temperature, the refractive index resolution, that resulted equal to about 2×10^{-4} RIU, can be obtained from the bulk sensitivity (about 900 nm/RIU) and the max experimentally measured variation of the resonance wavelength (0.2 nm).

3.4 Cost modelling: numerical results

Based on the assumptions made so far in the model, the cost allocation was performed. The results are summarized in Table 5 and Fig. 19.

According with the results obtained from the implemented cost model, the material costs have the greatest impact on the splitter final cost (70% of the total). This result is justified by high cost of the raw materials used on the *Objet260 Connex 1* 3d printer, in that Stratasys uses closed machine with proprietary materials. Conversely, power costs

and depreciation have a low impact on the total cost, respectively equal to 3% and 27% of the total cost.

4 Conclusions

In this work, a multiparameter SPR sensor for simultaneous refractive index and temperatures measurements, by exploiting two different channels properly tailored with different metals coatings, was developed by following a novel planar approach, which was already proposed by the authors for a simple SPR sensor [32].

The proposed sensing approach relative to the simultaneous monitoring of these two parameters is particularly advantageous when dealing with biosensors based on SPR. In this case, the bulk solution and the binding properties are strongly influenced by temperature environment variations. So, the proposed sensors could be used in this application field.

The SPR multiparameter sensor was fully designed and manufactured by using a standard inkjet 3D printing and commercial resins having suitable refractive index values, especially in terms of combination for core and cladding.

The profile monitoring analysis used as quality control method for the dimensional accuracy and correctness of the designed 3D CAD model resulted to be a cost-effective approach, which revealed no issues for the quality of the manufactured parts by using the chose inkjet 3D printing method. Indeed, small process deviations among profiles were detected, so obtaining a high process capability, which confirms the suitability of the selected manufacturing technique for a mass production.

The multiparameter SPR sensor was numerically and experimentally tested, and the results confirm that its performances, in terms of bulk sensitivity, are even better than other SPR sensors previously proposed in other experimental works.

The cost modelling resulted in an overall cost of 23€ for the developed device, so proving its low-cost manufacturing if compared with other traditional SPR sensor. However, being this cost mainly related to the high cost of *Stratasys* raw materials, it can be decreased in further studies by using cheaper photocurable resins which have already been developed by several companies for vat photopolymerization 3D printing.

Furthermore, to minimize mass and manufacturing costs, design optimization methods, such as *generative design* and *topology optimization*, are essential. These methods enable the fabrication of complex geometric models that are difficult or impossible to produce by using conventional manufacturing technologies. To carry out an optimization for the sensor's shape, we have to preserve the waveguide cores and the hole-pin systems, incorporating these bodies in the final

shape of the design, and model the part of the sensors as lightweight structures, such as trabecular or lattice design, according to the load and external constraints.

In conclusion, all the obtained results in terms of performances, quality control, and cost modelling are sufficient to assess that the developed sensor is suitable as a novel biochemical multiparameter sensor for disparate applications in biological, chemical, and environmental industries. So, several kinds of novel SPR sensors which work as SPR array for simultaneous measurements of different parameters (number of channels bigger than two) can be further developed using the proposed approach, especially by exploiting either different combination of metal coatings for each device's channel or even *n*-layers of different noble metals to tailor the same channel.

Finally, further investigation of quality engineering techniques applied to the proposed 3D printing process is worth of investigation, as well. In particular, the selection of proper quality *monitoring* techniques for small production runs with a finite production horizon of customized parts, as it usually occurs in additive manufacturing, must be carefully considered. For example, distribution-free control charts are suggested for application, thanks to the fact that they can immediately started at the beginning of the production. Furthermore, the investigation of quality *improvement* approaches based on efficient design of experiments (DoE) on the most important process parameters should be carefully considered, due to the very small number of parts available to be collected and measured at each production run.

Declarations

Ethics approval The paper does not request for ethics approval.

Consent for publication Yes.

Conflict of interest The authors declare no competing interests.

Disclaimer The funders had no role in the design of the study; in the collection, analyses, or interpretation of data; in the writing of the manuscript, or in the decision to publish the results.

References

1. Zhang Z, Zhao P, Sun F et al (2007) Self-referencing in optical-fiber surface plasmon resonance sensors. IEEE Photon Technol Lett 19:1958–1960. https://doi.org/10.1109/LPT.2007.909669
2. Li L, Li X, Xie Z et al (2012) Simultaneous measurement of refractive index and temperature using thinned fiber based Mach-Zehnder interferometer. Opt Commun 285:3945–3949. https://doi.org/10.1016/j.optcom.2012.05.060
3. Flores-Bravo JA, Fernandez R, Antonio Lopez E et al (2021) Simultaneous sensing of refractive index and temperature with supermode interference. J Light Technol 39:7351–7357. https://doi.org/10.1109/JLT.2021.3113863
4. Yu X, Chen X, Bu D et al (2016) In-fiber modal interferometer for simultaneous measurement of refractive index and temperature. IEEE Photonics Technol Lett 28:189–192. https://doi.org/10.1109/LPT.2015.2489559
5. Zhang W, Wu X, Wu X et al (2021) Simultaneous measurement of refractive index and temperature or temperature and axial strain based on an inline Mach-Zehnder interferometer with TCF–TF–TCF structure. Appl Opt 60:1522–1528. https://doi.org/10.1364/AO.417124
6. Wang F, Pang K, Ma T et al (2020) Folded-tapered multimode-no-core fiber sensor for simultaneous measurement of refractive index and temperature. Opt Laser Technol 130:106333. https://doi.org/10.1016/j.optlastec.2020.106333
7. Bai Y, Yin B, Liu C et al (2014) Simultaneous measurement of refractive index and temperature based on NFN Structure. IEEE Photonics Technol Lett 26:2193–2196. https://doi.org/10.23919/PS.2019.8817732
8. Dong Y, Xiao S, Wu B et al (2019) Refractive index and temperature sensor based on D-shaped fiber combined with a fiber bragg grating. IEEE Sens J 19:1362–1367. https://doi.org/10.1109/JSEN.2018.2880305
9. Meng H, Shen W, Zhang G et al (2010) Fiber Bragg grating-based fiber sensor for simultaneous measurement of refractive index and temperature. Sensors Actuators, B Chem 150:226–229. https://doi.org/10.1016/j.snb.2010.07.010
10. Zawisza R, Eftimov T, Mikulic P, et al (2018) Ambient refractive-index measurement with simultaneous temperature monitoring based on a dual-resonance long-period grating inside a fiber loop mirror structure. Sensors (Switzerland) 18. https://doi.org/10.3390/s18072370
11. Zheng J, Liu B, Zhao L, et al (2022) An optical sensor designed from cascaded anti-resonant reflection waveguide and fiber ring-shaped structure for simultaneous measurement of refractive index and temperature. IEEE Photonics J 14. https://doi.org/10.1109/JPHOT.2022.3144156
12. Hu Y, Lin Q, Yan F et al (2020) Simultaneous measurement of the refractive index and temperature based on a hybrid fiber interferometer. IEEE Sens J 20:13411–13417. https://doi.org/10.1109/JSEN.2020.3006089
13. Huang J, Lan X, Kaur A et al (2014) Temperature compensated refractometer based on a cascaded SMS/LPFG fiber structure. Sensors Actuators, B Chem 198:384–387. https://doi.org/10.1016/j.snb.2014.03.062
14. Ma T, Yuan J, Sun L, et al (2017) Simultaneous measurement of the refractive index and temperature based on microdisk resonator

with two whispering-gallery modes. IEEE Photonics J 9. https://doi.org/10.1109/JPHOT.2017.2648259

15. Hu T, Zhao Y, Song A (2016) Fiber optic SPR sensor for refractive index and temperature measurement based on MMF-FBG-MMF structure. Sensors Actuators, B Chem 237:521–525. https://doi.org/10.1016/j.snb.2016.06.119

16. Zhang P, Lu B, Sun Y et al (2019) Side-polished flexible SPR sensor modified by graphene with in situ temperature self-compensation. Biomed Opt Express 10:215. https://doi.org/10.1364/boe.10.000215

17. Velázquez-González JS, Monzón-Hernández D, Moreno-Hernández D et al (2017) Simultaneous measurement of refractive index and temperature using a SPR-based fiber optic sensor. Sensors Actuators, B Chem 242:912–920. https://doi.org/10.1016/j.snb.2016.09.164

18. Xianchao Y, Ying L, Baolin L, Jianquan Y (2017) Simultaneous measurement of refractive index and temperature based on SPR in D-shaped MOF. Appl Opt 56:4369–4374. https://doi.org/10.23919/PS.2019.8817732

19. Liu L, Zheng J, Deng S, et al (2021) Parallel polished plastic optical fiber-based spr sensor for simultaneous measurement of ri and temperature. IEEE Trans InstrumMeas 70. https://doi.org/10.1109/TIM.2021.3072136

20. Wang J-K, Ying Y, Gao Z, et al (2022) Double-sided photonic crystal fiber (PCF) temperature and refractive index (RI) sensor based on surface plasmon resonance (SPR). 1–15. https://doi.org/10.1080/10739149.2022.2078835

21. Hoa XD, Kirk AG, Tabrizian M (2007) Towards integrated and sensitive surface plasmon resonance biosensors: a review of recent progress. Biosens Bioelectron 23:151–160. https://doi.org/10.1016/j.bios.2007.07.001

22. Fiorini GS, Chiu DT (2005) Disposable microfluidic devices: fabrication, function, and application. Biotechniques 38:429–446. https://doi.org/10.2144/05383RV02

23. Takezawa Y, Akasaka S, Ohara S et al (1994) Low excess losses in a Y-branching plastic optical waveguide formed through injection molding. Appl Opt 33:2307. https://doi.org/10.1364/ao.33.002307

24. Park H-J (2011) Low-cost 1×2 plastic optical beam splitter using a V-type angle polymer waveguide for the automotive network. Opt Eng 50:075002. https://doi.org/10.1117/1.3595428

25. Klotzbuecher T, Braune T, Dadic D et al (2003) Fabrication of optical 1x2 POF couplers using the laser-LIGA technique. Laser Micromach Optoelectron Device Fabr 4941:121. https://doi.org/10.1117/12.470165

26. Mizuno H, Sugihara O, Kaino T et al (2005) Compact Y-branch-type polymeric optical waveguide devices with large-core connectable to plastic optical fibers. Japanese J Appl Physics, Part 1 Regul Pap Short Notes Rev Pap 44:8504–8506

27. Ehsan AA, Shaari S, Rahman MKA (2008) Design and fabrication of an acrylic-based 1×2 POF coupler using CNC Machining. IEEE IntConf Semicond Electron Proceedings, ICSE 340–344. https://doi.org/10.1109/SMELEC.2008.4770337

28. Prajzler V, Neruda M, Špirková J (2013) Planar large core polymer optical 1x2 and 1x4 splitters connectable to plastic optical fiber. Radioengineering 22:751–757

29. Prajzler V, Kulha P, Knietel M, Enser H (2017) Large core plastic planar optical splitter fabricated by 3D printing technology. Opt Commun 400:38–42. https://doi.org/10.1016/j.optcom.2017.04.070

30. Cook K, Canning J, Leon-Saval S et al (2015) Air-structured optical fiber drawn from a 3D-printed preform. Opt Lett 40:3966. https://doi.org/10.1364/ol.40.003966

31. Luo Y, Canning J, Zhang J, Peng GD (2020) Toward optical fibre fabrication using 3D printing technology. Opt Fiber Technol 58:102299. https://doi.org/10.1016/j.yofte.2020.102299

32. Cennamo N, Saitta L, Tosto C, et al (2021) Microstructured surface plasmon resonance sensor based on inkjet 3d printing using photocurable resins with tailored refractive index. Polymers (Basel) 13. https://doi.org/10.3390/polym13152518

33. Budzik G, Woźniak J, Paszkiewicz A, et al (2021) Methodology for the quality control process of additive manufacturing products made of polymer materials. Materials (Basel) 14. https://doi.org/10.3390/ma14092202

34. Villarraga-Gómez H, (2018) The role of X-ray computed tomography in the 3D printing revolution. RAPID + TCT 2018 Conference, Fort Worth, Texas USA. https://doi.org/10.13140/RG.2.2.20154.70089

35. Dorweiler B, Baqué PE, Chaban R et al (2021) Quality control in 3D printing: accuracy analysis of 3D-printed models of patient-specific anatomy. Materials (Basel) 14:1–13. https://doi.org/10.3390/ma14041021

36. Khosravani MR, Reinicke T (2020) On the use of X-ray computed tomography in assessment of 3D-printed components. J Nondestruct Eval 39. https://doi.org/10.1007/s10921-020-00721-1

37. Mahmoud MA, Woodall WH (2004) Phase I analysis of linear profiles with calibration applications. Technometrics 46:380–391. https://doi.org/10.1198/004017004000000455

38. Xu Y, Wu X, Guo X et al (2017) The boom in 3D-printed sensor technology. Sensors 17:1166

39. Muñoz J, Pumera M (2020) Accounts in 3D-printed electrochemical sensors: towards monitoring of environmental pollutants. ChemElectroChem 7:3404–3413. https://doi.org/10.1002/celc.202000601

40. Drotning WD, Roth EP (1989) Effects of moisture on the thermal expansion of poly(methylmethacrylate). J Mater Sci 24:3137–3140. https://doi.org/10.1007/BF01139031

41. Vitoria I, Zamarreño CR, Ozcariz A, Matias IR (2021) Fiber optic gas sensors based on lossy mode resonances and sensing materials used therefor: a comprehensive review. Sensors (Switzerland) 21:1–26. https://doi.org/10.3390/s21030731

42. Del Villar I, Arregui FJ, Zamarreño CR et al (2017) Optical sensors based on lossy-mode resonances. Sensors Actuators, B Chem 240:174–185. https://doi.org/10.1016/j.snb.2016.08.126

43. Cennamo N, Arcadio F, Noel L et al (2021) Flexible and ultrathin metal-oxide films for multiresonance-based sensors in plastic optical fibers. ACS Appl Nano Mater 4:10902–10910. https://doi.org/10.1021/acsanm.1c02345